Manipulating antiferromagnetic interfacial states by spin-orbit torques

E. Z. Zhang,[1,2,*] Y. C. Deng,[1,2,*] X. H. Liu,[1,2,†] X. Z. Zhan,[3] T. Zhu,[3,4] and K. Y. Wang[1,2,5,6,‡]
[1]*State Key Laboratory for Superlattices and Microstructures, Institute of Semiconductors, Chinese Academy of Sciences, Beijing 100083, China*
[2]*Center of Materials Science and Optoelectronics Engineering, University of Chinese Academy of Sciences, Beijing 100049, China*
[3]*Spallation Neutron Source Science Center, Dongguan 523803, China*
[4]*Beijing National Laboratory for Condensed Matter Physics and Institute of Physics, Chinese Academy of Sciences, Beijing 100190, China*
[5]*Beijing Academy of Quantum Information Sciences, Beijing 100193, China*
[6]*Center for Excellence in Topological Quantum Computation, University of Chinese Academy of Science, Beijing 100049, China*

(Received 12 August 2021; accepted 4 October 2021; published 12 October 2021)

We systematically investigated the manipulation of antiferromagnetic interfacial states through current-induced spin-orbit torques (SOT) in the Pt/Co/$Ir_{25}Mn_{75}$(Ir-Mn) system with varying Ir-Mn or Co thickness. The high tunability of antiferromagnetic interfacial states, that the antiferromagnetic interfacial spins gradually switched from upward to downward or vice versa by SOT, was achieved for the samples with $t_{IrMn} \geqslant 4$nm, whereas the switching ability of antiferromagnetic interfacial spins via SOT under a perpendicular field or a longitudinal field was different, which was attributed to the influence from partial canted interfacial spins. Moreover, the interfacial spins of Ir-Mn layer can be also effectively tuned by SOT across Ru layer in the Pt/Co/Ru/Ir-Mn system, where the exchange coupling between Co and Ir-Mn decreased with increasing the thickness of the Ru layer. Our work provides a comprehensive understanding for manipulating antiferromagnetic interfacial states via SOT, which will promote innovative designs for antiferromagnetic spintronic devices.

DOI: 10.1103/PhysRevB.104.134408

I. INTRODUCTION

With the development of information technology, spintronic devices with high storage density, low power consumption, large scalability, and high write/read speed are urgently desired. In the past several years, the antiferromagnetic (AFM) materials have attracted extensive interest due to their distinct advantages compared to the ferromagnets: robust against external magnetic fields, absence of stray fields, ultrafast dynamics, and theoretically predict strong spin-transfer torque capability [1–10]. Furthermore, there exists a wide range of AFM materials including insulators, metals, semimetals, semiconductors, or superconductors [1–3,11,12]. In particular, the recent discovery of electrical switching and readout of an antiferromagnet by current-induced spin-orbit torque (SOT) demonstrates that antiferromagnets can be electrically manipulated in similar ways to their ferromagnetic (FM) counterparts [13]. This opens the possibility to uncover a multitude of known and newly identified unique features of antiferromagnets for spintronics researches and applications.

Yet, it is worth pointing out that most previous work focused on electrical manipulation of bulk properties of AFM materials [4–10,13]. As an important part of antiferromagnets, the interfacial behaviors controlled by electrical current attract far less attention [14–16]. How to manipulate the antiferromagnetic interfacial spins effectively is very important for practical applications of AFM spintronics. As a unique tool to directly reflect the antiferromagnetic interfacial states, exchange bias (EB) originates from the exchange coupling of the magnetic spins in an antiferromagnet to the magnetization in an adjacent ferromagnet, which induces a preferred direction for magnetization of ferromagnet and thereby allows establishing a reference magnetization direction [17–20]. In previous work, the electrical control of EB in FM/AFM heterostructures using insulating multiferroic $YMnO_3$, $BiFeO_3$, or Cr_2O_3 as the dielectric layer has been investigated [21–23], whereas this effective electrical control faces a challenge for metallic AFM materials, such as Ir-Mn, Fe-Mn, or Pt-Mn.

Here, we systematically investigated the manipulation of antiferromagnetic interfacial states via electrical current in the Pt/Co/$Ir_{25}Mn_{75}$(Ir-Mn) system. The high adjustability of antiferromagnetic interfacial states by SOT was realized for the samples with $t_{IrMn} \geqslant 4$ nm, while the switching ability of antiferromagnetic interfacial spins through SOT was different using a perpendicular field or a longitudinal field. Furthermore, the manipulation of antiferromagnetic interfacial states by SOT was also studied in the Pt/Co/Ru/Ir-Mn system with varying the thickness of the Ru layer. The precise tunability of antiferromagnetic interfacial states through SOT offers a very efficient route to improve the spintronics functionalities in antiferromagnets.

II. EXPERIMENT

Three series stack structures of Ta(1)/Pt(3)/Co(0.8)/$Ir_{25}Mn_{75}(t)$/Ta(2) (thickness in nanometers) with $t_{IrMn} = 2$, 3, 4, 5, 6, 8, and 10 nm, Ta(1)/Pt(3)/Co(t)/$Ir_{25}Mn_{75}$(6)/Ta(2) with $t_{Co} = 0.6$, 0.7, 0.8, 0.9, 1.0, and 1.2 nm, and

*These authors contributed equally to this work.
†xionghualiu@semi.ac.cn
‡kywang@semi.ac.cn

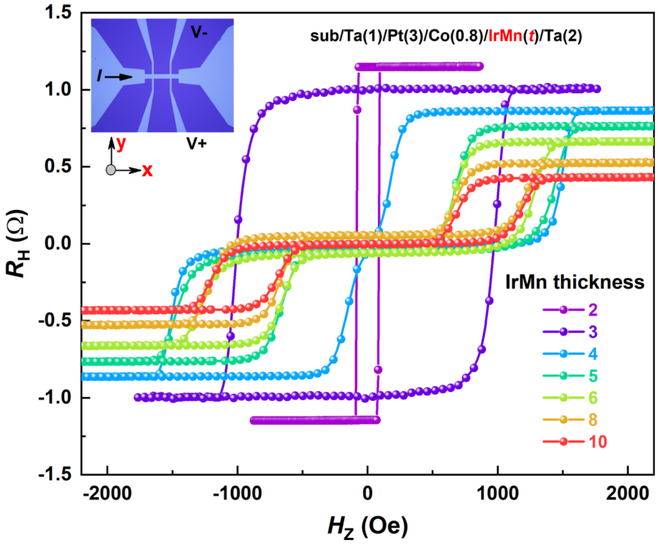

FIG. 1. Initial R_H vs H_z curves for samples Ta(1)/Pt(3)/Co(0.8)/$Ir_{25}Mn_{75}$(t)/Ta(2) with $t_{IrMn} = 2$, 3, 4, 5, 6, 8, and 10 nm, before applying pulsed currents. A square hysteresis loop is found for $t_{IrMn} = 2$ and 3 nm, while two-step magnetization switching is observed for $t_{IrMn} \geqslant 4$ nm. Inset: The optical micrograph of a typical Hall bar with the definition of the coordinate system and the measurement method.

Ta(1)/Pt(3)/Co(1)/Ru(t)/$Ir_{25}Mn_{75}$(6)/Ta(2) with $t_{Ru} = 0.2$, 0.4, 0.6, 0.8, 1.0, and 1.2 nm, were deposited on thermally oxidized Si substrate by magnetron sputtering at room temperature. The bottom and top Ta layers were used for adhesion and capping layers, respectively. The base pressure was less than 1×10^{-8} Torr before deposition, and the Ar pressure of the sputtering chamber was 0.8 mTorr during deposition. The deposited rates for Ta, Pt, Co, Ru, and $Ir_{25}Mn_{75}$ (Ir-Mn) films were controlled to be ≈0.016, 0.025, 0.012, 0.011, and 0.015 nm/s, respectively [24]. After that, the samples were patterned into Hall bar devices with channel width of 10 μm by photolithography and Ar-ion etching. For field-annealing treatments, the fabricated devices were annealed at 250 °C for 30 min at a base vacuum of 1×10^{-7} Torr under an out-of-plane magnetic field of 5 kOe, then were field cooled to room temperature, by using vacuum furnace for magnetic-field annealing (F800-35, East Changing Technologies, China).

The optical micrograph of a typical Hall bar with the definition of the coordinate system and the measurement method are presented as an inset of Fig. 1. The Kerr characterization of magnetization hysteresis was taken using a NanoMoke3 magneto-optical Kerr magnetometer. The anomalous Hall effect measurements were carried out at room temperature with Keithley 2602 as the sourcemeter and Keithley 2182 as the nanovoltage meter.

Polarized neutron reflectivity (PNR) measurements on Ta/Pt/Co/Ir-Mn/Ta samples were conducted on the multipurpose reflectometer beamline at the Chinese Spallation Neutron Source. The specular reflectivities were measured at room temperature as a function of the wave-vector transfer along the film surface normal. R^{++} and R^{--} represent the reflectivities from the spin-up and spin-down polarized neutrons, respectively. PNR data were fitted using GENX software.

III. ANTIFERROMAGNETIC THICKNESS DEPENDENCE

The magnetic parameters of antiferromagnets were reported to change with varying thickness, including blocking temperature, rotation of easy axis, etc. [2,3], which will greatly affect the magnetic properties of FM/AFM bilayers. We firstly investigated the electrical current manipulation of antiferromagnetic interfacial states with AFM thickness. Figure 1 shows the anomalous Hall resistance (R_H) as a function of out-of-plane field (H_z) for as-grown samples Ta(1)/Pt(3)/Co(0.8)/$Ir_{25}Mn_{75}$(t)/Ta(2) with $t_{IrMn} = 2$, 3, 4, 5, 6, 8, and 10 nm, before applying pulsed currents. A square hysteresis loop with no EB is observed for devices with $t_{IrMn} = 2$ or 3 nm. With increasing $t_{IrMn} \geqslant 4$ nm, the R_H vs H_z curves exhibit two-step magnetization reversal behavior.

A series of variations of magnetic parameters of samples with t_{IrMn} are presented in Fig. 2. The full and minor hysteresis loops of sample with $t_{IrMn} = 6$ nm is displayed in Fig. 2(a), where the exchange-bias field (H_E) and coercivity field (H_C) are defined as $H_E = H_L + (H_R - H_L)/2 = (H_R + H_L)/2$ and $H_C = (H_R - H_L)/2$, respectively (marked with the arrows), and the saturation field (H_S) is indicated by arrow as well. The H_S, H_C, and H_E dependence of t_{IrMn} are summarized in Figs. 2(b)–2(d), respectively. Square hysteresis loops without EB are only found for the samples with $t_{IrMn} = 2$ and 3 nm, the H_C and H_E of which are not included in Figs. 2(b)–2(d), respectively.

Obviously, the H_S [Fig. 2(b)] and H_C [Fig. 2(d)] are maximum for $t_{IrMn} = 4$ nm and then gradually decrease with further increasing t_{IrMn}, implying the gradual reduction of effective perpendicular anisotropy of the samples with $t_{IrMn} > 4$ nm [19]. Meanwhile the H_E appears for $t_{IrMn} = 4$ nm, and sharply jumps to about 1 kOe for $t_{IrMn} = 5$ nm. With the increase of t_{IrMn}, this value slightly reduces to 936 Oe [Fig. 2(c)]. It has been reported that the EB can be affected by many factors in the FM/AFM system, such as the FM magnetization (M_{FM}), the thickness of FM layer t_{FM}, the anisotropy and exchange stiffness of AFM (K_{AFM} and A_{AFM}), and the exchange-bias field is proposed as $H_E \propto (K_{AFM}A_{AFM})^{1/2}/M_{FM}t_{FM}$ [19,20,25]. Thus, the variation of H_E with t_{IrMn} is mainly related to the change of K_{AFM} for constant FM layer.

Indeed, the easy axis of thin Ir-Mn film was reported to be rotated due to the strong interfacial coupling of the FM/AFM system [26,27]. With increasing t_{IrMn}, the enhanced AFM anisotropy energy ($K_{AFM}t_{AFM}$) induces gradual rotation of easy axis (bulk) from out-of-plane to in-plane direction [26–29]; the perpendicular component of K_{AFM} gradually decreases, generating the gradual reduction of H_E. Notably, the minimum H_E corresponds to the maximum H_C for $t_{IrMn} = 4$ nm [Figs. 2(c) and 2(d)], while the maximum H_E is observed for $t_{IrMn} = 5$ nm [Fig. 2(c)].

For the thinner Ir-Mn case ($t_{IrMn} = 4$ nm), more Ir-Mn interfacial spins rotating together with Co during the hysteresis loop measurement produces a smaller H_E but great enhancement of H_C [19,20]. The thicker t_{IrMn} results in fewer interfacial spins of Ir-Mn layer rotating with Co and hence larger H_E and smaller H_C. On the other hand, the weakened perpendicular component of K_{AFM} produces a reduction of H_E with increasing t_{IrMn}; thus, $t_{IrMn} = 5$ nm can be considered as a critical thickness which can balance these two effects.

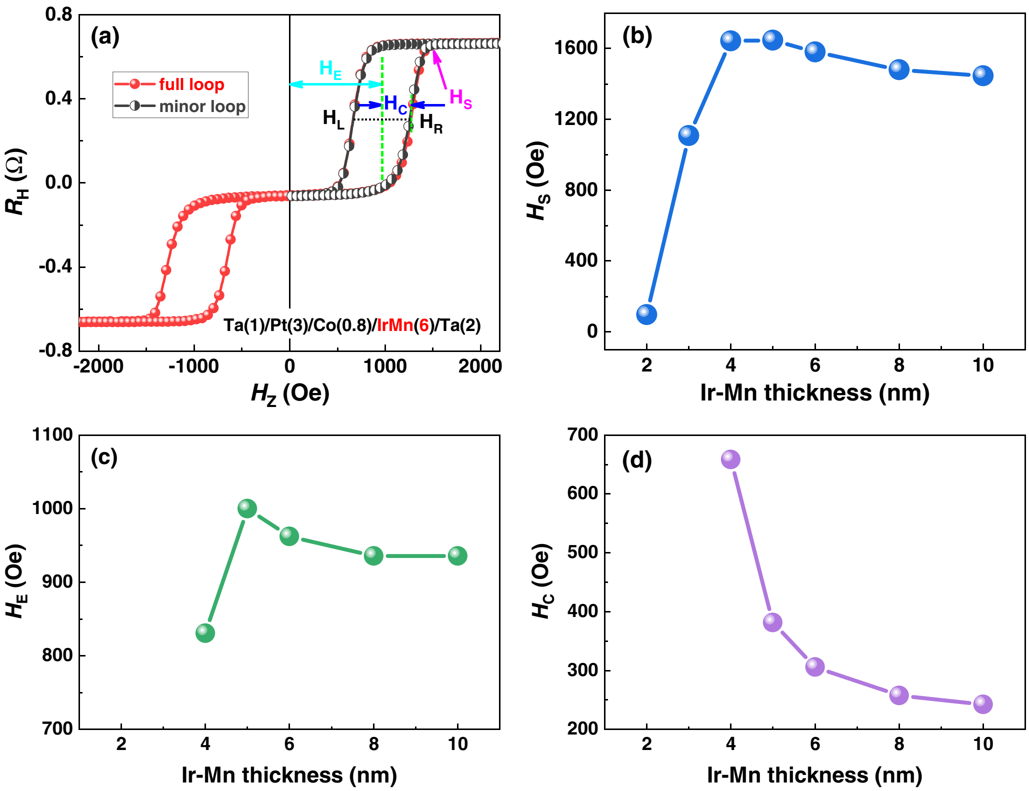

FIG. 2. (a) Initial full and minor R_H vs H_z curves for sample $Ta(1)/Pt(3)/Co(0.8)/Ir_{25}Mn_{75}(6)/Ta(2)$. The H_S, H_E, and H_C are indicated by arrows. The H_S, H_E, and H_C dependence of t_{IrMn} are exhibited in (b)–(d), respectively.

In addition, two competing interactions exist with changing t_{IrMn}: the one between AFM/FM spins causes antiferromagnetic interfacial spins along out-of-plane, and the other one between bulk and interfacial AFM spins prefers in-plane interfacial spins. This competition will induce the formation of perpendicular antiferromagnetic interfacial spins for thicker t_{IrMn} [14,15]. For as-grown samples, there is no preference between upward and downward pinning directions because both are along the easy axis of the Co layer, leading to the two-step R_H vs H_z curves in Fig. 1. Therefore, the antiferromagnetic interfacial states can be revealed by the behaviors of R_H vs H_z curves.

IV. MANIPULATING ANTIFERROMAGNETIC INTERFACIAL STATES

Then we focused on manipulation of antiferromagnetic interfacial states by electrical current. The as-grown samples were then subjected to a sequence of current pulses along the x direction, by varying amplitude I_p at fixed width of 50 ms, in a longitudinal applied field of $H_x = 1$ kOe (see inset of Fig. 1). Through the spin Hall effect, a charge current in the $\pm x$ direction should generate a spin polarization along the $\pm y$ direction for positive spin Hall angle of Pt [30]. Such spin current can switch the magnetization of perpendicular magnetic anisotropy (PMA) Co between $\pm z$ direction, provided that both current density and H_x are large enough. Moreover, the absorption of transverse spin currents is found to change with the thickness of FM, with a characteristic saturation length of 1.2 nm [31] (longer than 0.8 nm in this system). Thus, not only the Co layer, but the antiferromagnetic interfacial spins can be also directly affected by SOT [14,15]. To clearly present the variation of antiferromagnetic interfacial states via SOT, different current pulses are exerted on the devices under $H_x = 1$ kOe.

Figure 3 shows the R_H vs H_z curves of sample with $t_{IrMn} = 6$ nm for initial state (a) and after applying current pulse $I_p = 20$ mA (b), 22 mA (c), 23 mA (d), 24 mA (e), and 26 mA (f) under $H_x = 1$ kOe, respectively. In this process, first, we set $H_x = 1$ kOe and then apply a single pulse I_p; after that, we set $H_x = 0$ and $I_p = 0$ and measure the R_H vs H_z loop. Clearly, the left minor loop gradually becomes bigger while the right one gradually shrinks with increasing I_p, indicating more antiferromagnetic interfacial spins are switched to upward by SOT, as schematically illustrated in the insets of Figs. 3(a) and 3(f) [15]. Furthermore, the H_E gradually reduces with increasing I_p (marked with a dashed line). Similarly, the enhanced negative I_p will induce the opposite trend: the right minor loop becomes bigger while the left one gradually shrinks, and H_E decreases with increasing negative I_p. The similar phenomena are observed for all the samples with $t_{IrMn} \geqslant 4$ nm.

The H_E and H_C as a function of I_p for the sample with $t_{IrMn} = 6$ nm are summarized in Figs. 4(a) and 4(b), respectively. The value of H_E sharply reduces from 976 Oe for $I_p = 19$ mA to 746 Oe for 24 mA and then slightly decreases to a saturation value of about 714 Oe for 28 mA. As $H_E \propto (K_{AFM}A_{AFM})^{1/2}/M_{FM}t_{FM}$, the change of H_E with I_p could be due to the variation of K_{AFM} for the constant FM and AFM thickness. One plausible scenario can be proposed: for initial state, the antiferromagnetic interfacial states possess

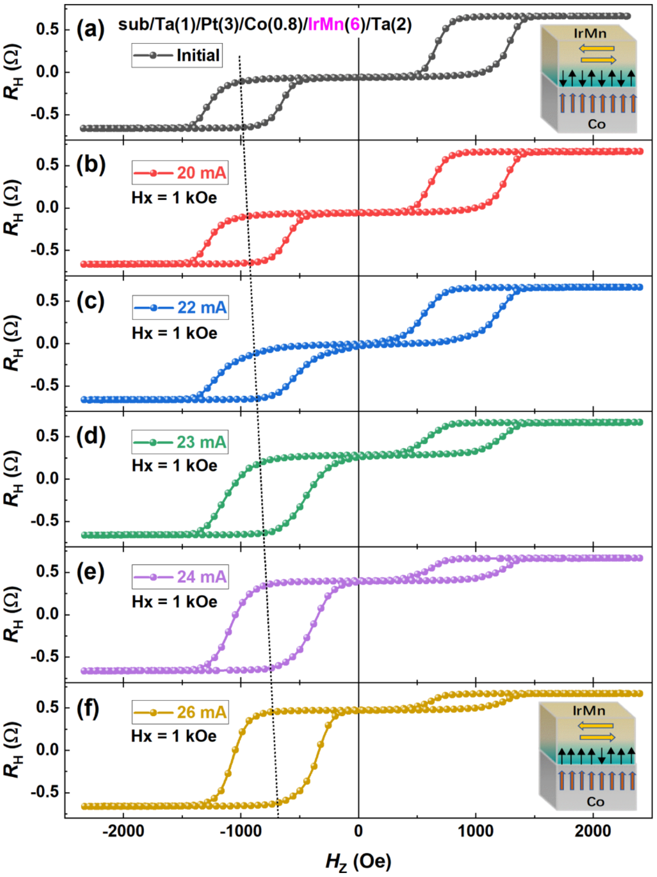

FIG. 3. R_H vs H_z curves for initial state (a) and after applying $I_p = 20\,\text{mA}$ (b), 22 mA (c), 23 mA (d), 24 mA (e), and 26 mA (f) under $H_x = 1\,\text{kOe}$, respectively, of sample Ta(1)/Pt(3)/Co(0.8)/$Ir_{25}Mn_{75}$(6)/Ta(2). The left minor loop gradually becomes bigger while the right one gradually shrinks, and the center of the left hysteresis loop gradually shifts to smaller field (indicated by a dashed line), with increasing I_p. Schematic configurations of AFM and FM layers with corresponding R_H vs H_z curves are presented as insets of (a) and (f), respectively.

nearly equivalent upward and downward spins [see inset of Fig. 3(a)], and the effective interfacial K_{AFM1} is maximum. After applying I_p, current-induced SOT acting on antiferromagnetic interfacial spins consists of a dampinglike torque $\mathbf{m} \times (\sigma \times \mathbf{m})$ (along the y direction) and a fieldlike torque $\mathbf{m} \times \sigma$ (along the x direction), where $\mathbf{m}$ is interfacial spin moment of the AFM layer and $\boldsymbol{\sigma}$ is the spin polarization of spin current [32–34]. This effect can switch antiferromagnetic interfacial spins to upward (downward) for positive (negative) I_p, which actually weakens the K_{AFM1}, resulting in the decrease of H_E.

The H_E for initial and saturation (after applying large enough I_p) cases for samples with different t_{IrMn} are plotted in Fig. 4(c). Compared to the initial state, the values of H_E for saturation state obviously reduce for all the samples. Interestingly, the minimum $\Delta H_E = H_{E\text{-initial}} - H_{E\text{-saturation}}$ [see inset of Fig. 4(c)] is observed for the so-called critical AFM thickness 5 nm. On the other hand, the H_C keeps nearly constant with I_p [see Fig. 4(b)] because the effective perpendicular anisotropy of sample varies very little via SOT, and similar results are observed for different t_{IrMn} shown in Fig. 4(d).

Figure 5(a) presents the R_H vs I_p curves under $H_x = 1\,\text{kOe}$ for different ultimate I_p of sample with $t_{IrMn} = 6\,\text{nm}$. The FM switching magnitude $\Delta R_H = R_H{}^+ - R_H{}^-$ gradually enlarges with increasing I_p, and becomes nearly saturated for $I_p \geqslant 26\,\text{mA}$. Figure 5(b) exhibits the R_H vs H_z curves after applying 28 and −28 mA under $H_x = 1\,\text{kOe}$, respectively. Both curves have a big and a small hysteresis loop; the main part of R_H vs H_z loop displays positive and negative H_E for 28 and −28 mA, respectively. Thus, the positive (negative) I_p switched most antiferromagnetic interfacial spins to upward (downward) [15]. While the existence of a small hysteresis loop for saturation I_p under $H_x = 1\,\text{kOe}$ (similar results are also observed for $H_x > 1\,\text{kOe}$) suggests that partial upward or downward antiferromagnetic interfacial spins could not be switched by SOT under H_x. Accordingly, the saturation FM switching of the R_H vs I_p curve only takes place between two steps of corresponding R_H vs H_z curves, indicating by the dashed lines in Figs. 5(a) and 5(b).

We then employed the PNR to reveal the reason for this phenomenon. Figure 6(a) shows the results of the room-temperature PNR measurements under the in-plane external field of 9 kOe. The inset plots the spin asymmetry, SA = $(R^{++} - R^{--})/(R^{++} + R^{--})$, where the R^{++} and R^{--} are the reflectivities for polarized neutron parallel or antiparallel to the external field. Although the PNR is only sensitive to in-plane magnetization [35], the R^{++} and R^{--} separate under a large in-plane external field because the perpendicular magnetized Co layer is pulled back along the plane of film. Figure 6(b) displays the theoretical model of sample's depth-resolved nuclear and magnetic scattering length density (nSLD and mSLD) as a function of the perpendicular momentum transfer vector Q.

The calculated curves shown in Fig. 6(a) are well consistent with the experimental results. An induced magnetization (0.38 μ_B) can be obtained in the Pt layer due to the proximity effect [36]. The Ir-Mn has an interfacial layer adjacent to Co, named Ir-Mn-Int, which may be due to the uncompensated pinned Mn spins at the interface of Ir-Mn [37]. From the fitting results, the magnetization of Ir-Mn-Int is about −0.1 μ_B, and the magnetization direction of this interfacial Ir-Mn layer is antiparallel to the Co layer [38]. The magnetization of Co is about 0.9 μ_B. The reason is that the Co layer is not fully pulled back along the plane of the film when the external field of 9 kOe is smaller than the perpendicular anisotropy field of the film. However, the in-plane component of magnetization of Co is about 0.09 μ_B under the external field of 20 Oe. The results demonstrate the existence of canted Co spins (along in-plane direction) in our Ta/Pt/Co/Ir-Mn/Ta samples, which could be originated from the interfacial Dzyaloshinskii-Moriya interaction [39]. Therefore, it is clear that the interfacial spins with effective spin moments along the in-plane direction cannot be changed to the perpendicular direction through SOT under H_x, resulting in an obvious step in the R_H vs H_z curves in Fig. 5(b) for saturation I_p.

To achieve the higher tunability of antiferromagnetic interfacial states, that all the antiferromagnetic interfacial spins can be switched from upward to downward or vice versa, we further investigated the manipulation of antiferromagnetic

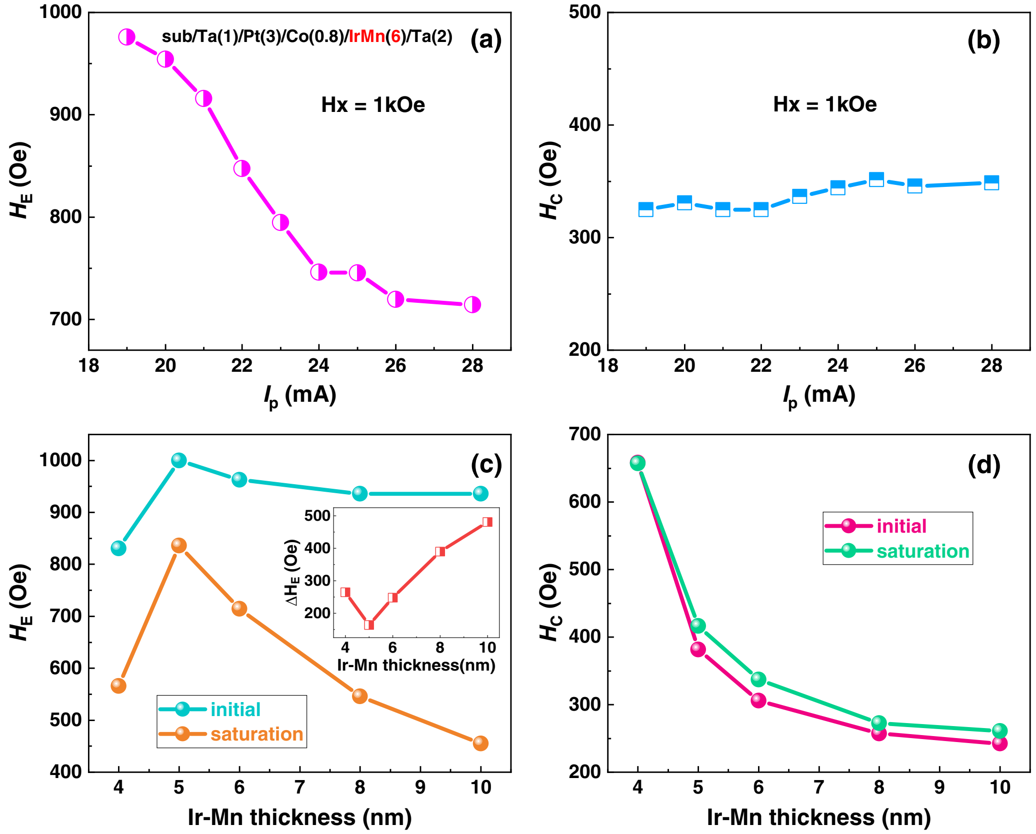

FIG. 4. (a) H_E and (b) H_C as a function of I_p (from 19 to 28 mA) under $H_x = 1$ kOe of sample Ta(1)/Pt(3)/Co(0.8)/$Ir_{25}Mn_{75}$(6)/Ta(2). The initial and saturation (exerted by large enough I_p and H_x) (c) H_E and (d) H_C dependence of t_{IrMn} for samples Ta(1)/Pt(3)/Co(0.8)/$Ir_{25}Mn_{75}$(t)/Ta(2) with $t_{IrMn} = 4$, 5, 6, 8, and 10 nm. Inset of (c) presents the ΔH_E vs t_{IrMn}, and the minimum ΔH_E is observed for the sample with $t_{IrMn} = 5$ nm.

interfacial states by SOT under H_z. As compared to the sample exerted by applying I_p and H_x, this way is more efficient, because the antiferromagnetic interfacial spins can be completely switched by SOT under H_z. Indeed, we can observe the evolution of antiferromagnetic interfacial spins from downward to upward (or vice versa) via SOT with varying H_z for all the samples with $t_{IrMn} \geqslant 4$ nm (similar phenomenon was also observed for the samples after applying variable I_p under constant H_z), which offers a precise way to manipulate the interfacial states of AFM layer.

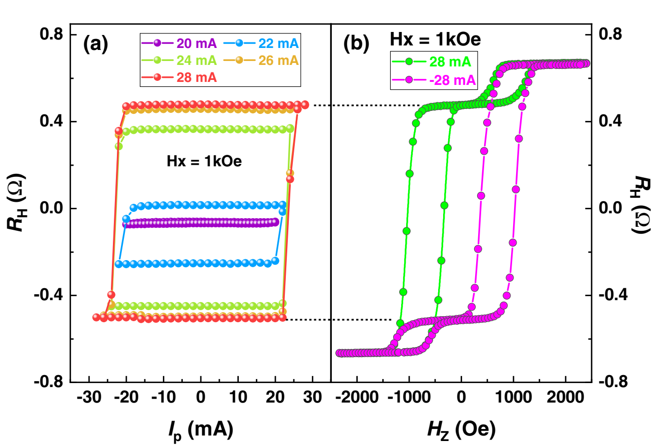

FIG. 5. (a) R_H vs I_p curves by applying different ultimate current pulses under fixed $H_x = 1$ kOe of sample Ta(1)/Pt(3)/Co(0.8)/ $Ir_{25}Mn_{75}$(6)/Ta(2). (b) R_H vs H_z curves after applying 28 (positive H_E) and −28 mA (negative H_E) under $H_x = 1$ kOe.

As shown in Fig. 7, the initial state is set by applying $I_p = 24$ mA under $H_z = 2$ kOe, and subsequent R_H vs H_z loops are obtaining after applying $I_p = 20$ mA of varying the magnitude of H_z. Clearly, the antiferromagnetic interfacial spins could be gradually flipped from upward to downward with enhancing negative H_z from −10 Oe to −2 kOe for the sample with $t_{IrMn} = 4$ nm. As a result, we successfully implemented the high adjustability of antiferromagnetic interfacial states via SOT under H_z or H_x, while the switching ability of antiferromagnetic interfacial spins via SOT is different under a perpendicular field or a longitudinal field because of the presence of canted interfacial spins.

V. FERROMAGNETIC THICKNESS DEPENDENCE

To further understand the manipulation of the antiferromagnetic interfacial states by SOT, we also investigated the samples with varying FM thickness: Ta(1)/Pt(3)/Co(t)/$Ir_{25}Mn_{75}$(6)/Ta(2) with $t_{Co} = 0.6$, 0.7, 0.8, 0.9, 1.0, and 1.2 nm. The initial R_H vs H_z curves for all the as-grown samples, before applying pulsed currents, are presented in Fig. 8. It is observed that the sample shows weak

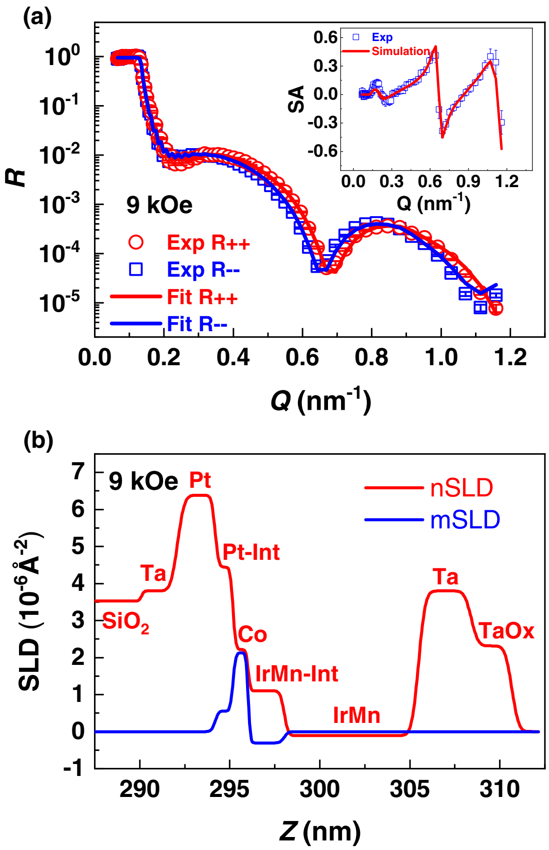

FIG. 6. (a) Polarized neutron reflectivity as a function of the perpendicular momentum transfer vector Q, and (b) the theoretical model of sample's depth-resolved nuclear and magnetic scattering length density (SLD) of sample Ta(1)/Pt(3)/Co(0.8)/$Ir_{25}Mn_{75}$(10)/Ta(2) Ta(1)/Pt(3)/Co(0.8)/$Ir_{25}Mn_{75}$(10)/Ta(2). Inset of (a): The spin asymmetry SA dependence of the perpendicular momentum transfer vector.

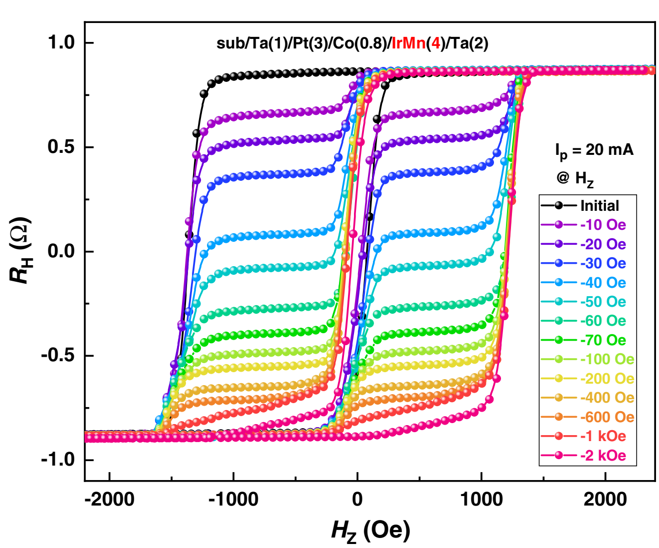

FIG. 7. R_H vs H_z curves after applying constant $I_p = 20$ mA under different H_z from −10 Oe to −2 kOe of sample Ta(1)/Pt(3)/Co(0.8)/$Ir_{25}Mn_{75}$(4)/Ta(2). A precise manipulation of AFM interfacial states via SOT under H_z is realized.

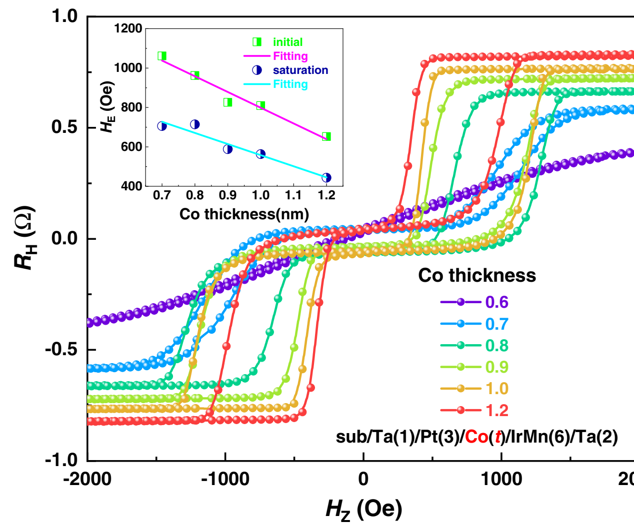

FIG. 8. Initial R_H vs H_z curves for samples Ta(1)/Pt(3)/Co(t)/$Ir_{25}Mn_{75}$(6)/Ta(2) with $t_{Co} = 0.6$, 0.7, 0.8, 0.9, 1.0, and 1.2 nm, before applying pulsed currents. The PMA is weak for very thin Co (0.6 nm) sample. Inset: H_E as a function of t_{Co} for initial and saturation (after applying large enough I_p under H_x) states. The linear variation of H_E with the increase of t_{Co} is observed for both cases.

PMA for very thin Co (0.6 nm) [40]. With increasing t_{Co} to 0.7 nm, the R_H vs H_z curve displays two-step magnetization switching with two narrow minor hysteresis loops, suggesting the slightly weak PMA. The samples have strong PMA with further increasing $t_{Co} \geqslant 0.8$ nm. From the equation $H_E \propto (K_{AFM}A_{AFM})^{1/2}/M_{FM}t_{FM}$, it is expected that the H_E should linearly vary with the increase of t_{Co} for a constant AFM layer; we do observe this phenomenon shown as an inset of Fig. 8.

Note that the apparent SOT-induced switching of antiferromagnetic interfacial spins, revealed by R_H vs H_z curves, is also found for the sample with $t_{Co} = 0.6$ nm although the PMA is very weak [see Fig. 9(a)]. On the other hand, for the sample with thick FM layer $t_{Co} = 1.2$ nm, the spin currents induced from Pt can pass through the Co layer to directly affect the antiferromagnetic interfacial states [31]. The positive (negative) H_E is observed for the device after applying $I_p = 28$ mA (−28 mA) under $H_x = 1$ kOe, as exhibited in Fig. 9(b). This means the characteristic saturation length of spin currents is in fact larger than 1.2 nm in our system. Furthermore, the precise adjustability of antiferromagnetic interfacial spins via SOT under H_z can be also obtained in this system.

VI. SPACER LAYER BETWEEN FERROMAGNETIC AND ANTIFERROMAGNETIC LAYERS

Having studied the manipulation of antiferromagnetic interfacial states through SOT with changing the thickness of the AFM or FM layer, to better make clear the related mechanism, we then came to investigate the switching of antiferromagnetic interfacial spins via SOT with inserting a nonmagnetic (NM) layer between FM and AFM layers. It has been reported that the exchange bias in FM/AFM is a long-range effect rather than the nearest-neighbor exchange coupling at the FM/AFM interface

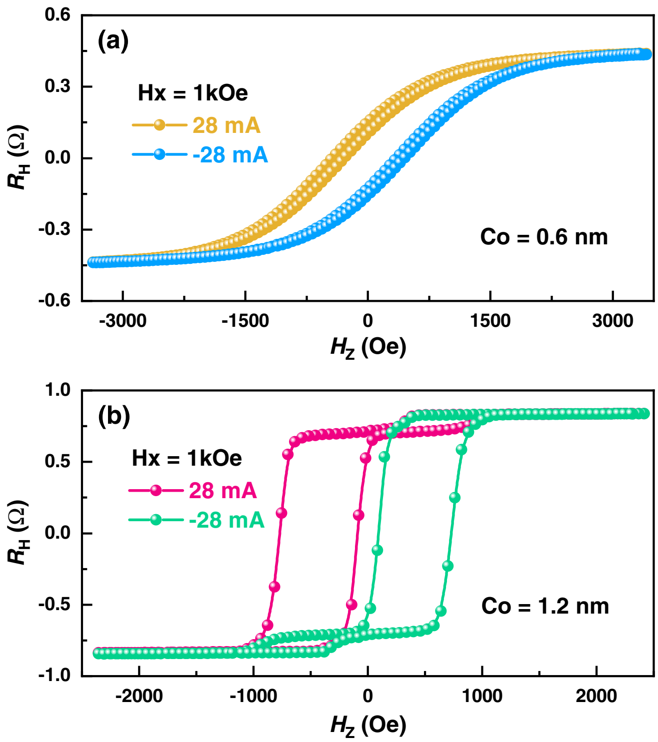

FIG. 9. R_H vs H_z curves for samples Ta(1)/Pt(3)/Co(t)/$Ir_{25}Mn_{75}$(6)/Ta(2) with $t_{Co} = 0.6$ (a) and 1.2 nm (b) after applying $I_p = 28$ and -28 mA under $H_x = 1$ kOe, respectively. The positive (negative) H_E for positive (negative) I_p is observed for both samples.

[41,42]. Therefore, the investigation on system of heavy-metal/FM/NM/AFM will present a further understanding of manipulating antiferromagnetic interfacial states by SOT. Figure 10 shows the initial R_H vs H_z curves for as-grown samples Ta(1)/Pt(3)/Co(1)/Ru(t)/$Ir_{25}Mn_{75}$(6)/Ta(2) with

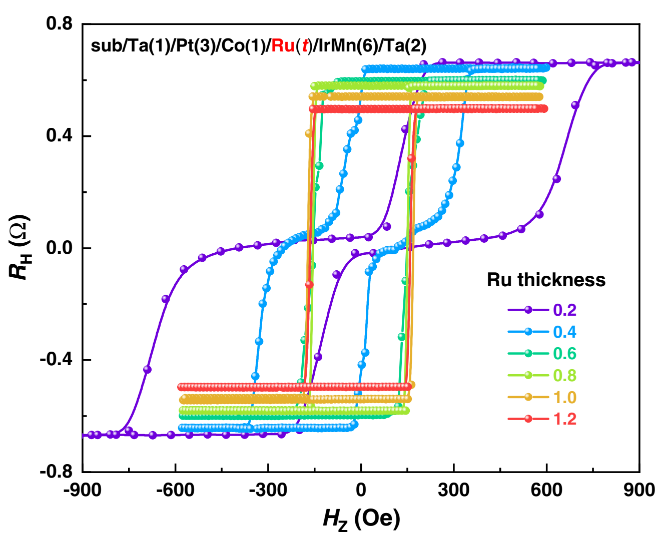

FIG. 10. Initial R_H vs H_z curves for samples Ta(1)/Pt(3)/Co(1)/Ru(t)/$Ir_{25}Mn_{75}$(6)/Ta(2) with $t_{Ru} = 0.2$, 0.4, 0.6, 0.8, 1.0, and 1.2 nm, before applying pulsed currents. By inserting spacer layer Ru between FM and AFM layers, the exchange coupling gradually weakens with increasing t_{Ru}.

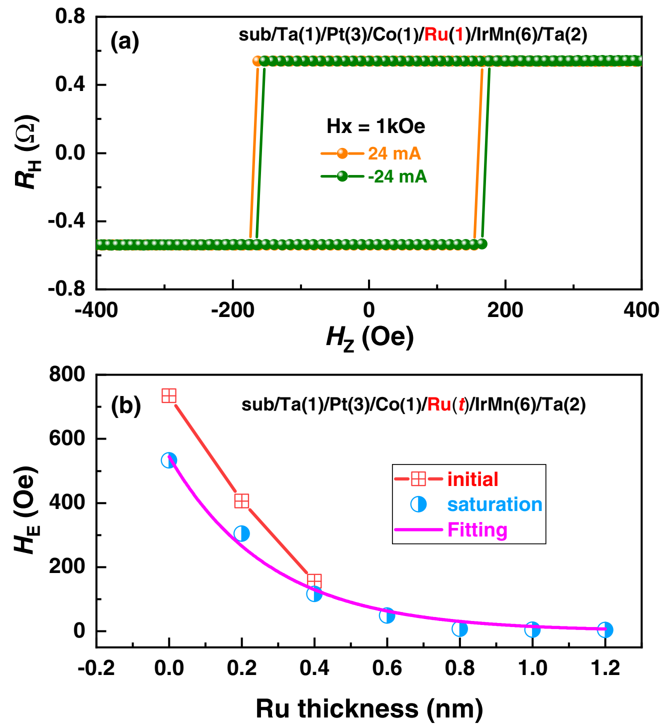

FIG. 11. (a) R_H vs H_z curves of sample Ta(1)/Pt(3)/Co(1)/Ru(1)/$Ir_{25}Mn_{75}$(6)/Ta(2) after applying $I_p = 24$ and -24 mA under $H_x = 1$ kOe. The positive (negative) H_E for positive (negative) I_p is observed. (b) H_E as a function of t_{Ru} for initial and saturation cases. The H_E with t_{Co} obeys an exponential decay with the equation $H_E \propto \exp(-t_{Ru}/L)$.

$t_{Ru} = 0.2$, 0.4, 0.6, 0.8, 1.0, and 1.2 nm, before applying pulsed currents. With increasing the thickness of the Ru spacer layer, the exchange coupling between Co and Ir-Mn weakens and thus the EB reduces. Correspondingly, the shape of R_H vs H_z curves varies from a two-step magnetization reversal behavior to a square hysteresis loop. For the samples with $t_{Ru} \geqslant 0.8$ nm, the two-step switching of R_H vs H_z curve completely disappears (H_E is zero).

Furthermore, the manipulation of antiferromagnetic interfacial spins through SOT was also found for these series samples. Figure 11(a) exhibits the R_H vs H_z curves after applying $I_p = 24$ and -24 mA under $H_x = 1$ kOe for the sample with $t_{Ru} = 1$ nm. It is clear that the positive (negative) H_E for positive (negative) I_p is observed although the value of H_E is small. Interestingly, compared to the R_H vs H_z curves in Fig. 5(b) and Fig. 9(b), the samples for thick Ru ($t_{Ru} \geqslant 0.8$ nm) do not have small minor hysteresis loop after applying saturation I_p under H_x, which implies that the influence from canted interfacial spins becomes very weak or even disappears. The H_E for initial (the EB is very weak for $t_{Ru} \geqslant 0.6$ nm; we thus only give out three points for thin Ru layer) and saturation (after applying large enough I_p under H_x) cases dependence of t_{Ru} is presented in Fig. 11(b). Similarly, the values of H_E for the samples exerted by SOT reduce as compared to the initial states. Moreover, the H_E for saturation case exponential decays with t_{Ru}, $H_E \propto \exp(-t_{Ru}/L)$ [Fig. 11(b)], where L is a constant which measures the range of the coupling [40].

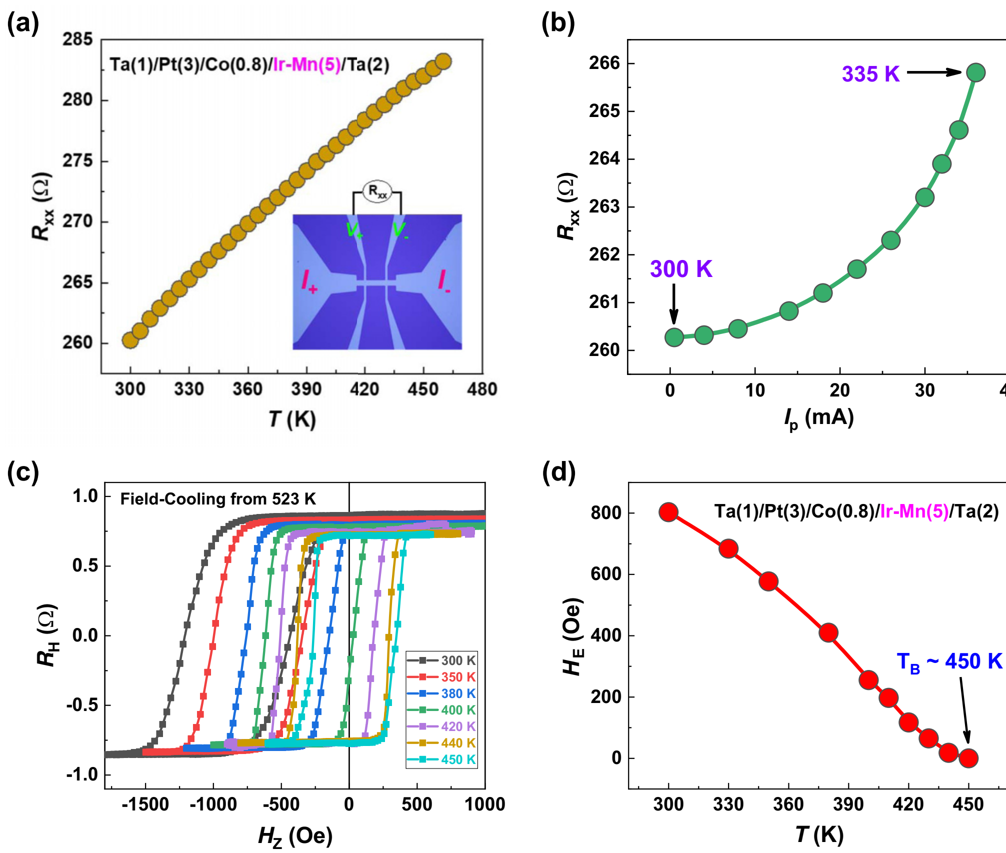

FIG. 12. Determination of the temperature increase due to Joule heating during the current pulse and the blocking temperature of the Ir-Mn layer for the sample Ta(1)/Pt(3)/Co(0.8)/$Ir_{25}Mn_{75}$(5)/Ta(2). (a) Longitudinal resistance as a function of temperature; inset presents the measurement scheme. (b) Resistance measured during the current pulse, vs the current pulse magnitude I_p for fixed pulse width of 50 ms. The temperature rise is about 35 K for $I_p = 36$ mA. (c) R_H vs H_z loops at different temperatures, after field cooling from 523 K. (d) Exchange-bias field (H_E) versus temperature extracted from the data in (c). The blocking temperature, defined as the temperature where the EB disappears, for 5 nm Ir-Mn layer is about 450 K.

This demonstrates that the SOT does not change the nature of exchange coupling in the FM/NM/AFM system. In addition, the SOT-induced switching of antiferromagnetic interfacial spins approximately disappears for the sample with $t_{Ru} = 1.2$ nm, where the thickness of $1(t_{Co}) + 1.2(t_{Ru}) = 2.2$ nm significantly exceeds the characteristic saturation length of spin currents across the spacer layer [14,15,31].

VII. JOULE HEATING

At last, the Joule heating is usually considered to be a very important issue in transport measurement process [43]. To check whether the observed antiferromagnetic interfacial spins switching is caused by current-induced Joule heating over the blocking temperature (T_B) of the Ir-Mn layer, we estimated the temperature rise due to Joule heating. We measured the longitudinal resistance (R_{xx}) as a function of temperature (from 300 to 460 K) for the sample Ta(1)/Pt(3)/Co(0.8)/$Ir_{25}Mn_{75}$(5)/Ta(2) shown in Fig. 12(a). Then the R_{xx} of the sample is measured during the current pulse, ranging from 0 to 36 mA, at 300 K [Fig. 12(b)]. By comparing this to the measured temperature dependence of resistance in Fig. 12(a), a temperature rise of about 35 K is estimated for a current pulse of 36 mA with 50-ms duration; see the arrows indicated in Fig. 12(b).

On the other hand, to determine the T_B of the Ir-Mn layer, the sample is field cooled from 523 K to room temperature under an out-of-plane magnetic field of 5 kOe. The R_H vs H_z curves after field cooling measured from 300 to 450 K are presented in Fig. 12(c). It is observed that the H_E gradually reduces with increasing temperature, and becomes zero at 450 K, as the data summarized in Fig. 12(d). Thus, the T_B for the 5-nm Ir-Mn sample, defined as the temperature where the EB disappears, is around 450 K, which is much higher than the current-induced temperature rise of about 35 K. Therefore, we can rule out a significant role of Joule heating in the observed switching.

VIII. CONCLUSION

In summary, we have systematically studied the manipulation of antiferromagnetic interfacial states via SOT in Pt/Co/Ir-Mn and Pt/Co/Ru/Ir-Mn systems. The high tunability of antiferromagnetic interfacial states by SOT under external fields was achieved for Pt/Co/Ir-Mn samples with $t_{IrMn} \geqslant 4$ nm, whereas, the switching ability of antiferromagnetic interfacial spins through SOT under H_z or H_x was different because of the presence of canted interfacial spins. In addition, the SOT-induced variations of antiferromagnetic interfacial states for Pt/Co/Ir-Mn samples with Co thickness were also investigated, where the controlling of antiferromagnetic interfacial states was observed for the samples from $t_{\mathrm{Co}} = 0.6$ to 1.2 nm. Furthermore, the manipulation of antiferromagnetic interfacial states via SOT was further studied in the Pt/Co/Ru/Ir-Mn system. With increasing Ru thickness, the exchange coupling between Co and Ir-Mn layers sharply decreases. The SOT can tune the switching of antiferromagnetic interfacial states but does not change the nature of exchange coupling in the Co/Ru/Ir-Mn system. At last, the effect of Joule heating was also investigated; our work indicated that the manipulation of antiferromagnetic interfacial states was originated from the SOT but not caused by current-induced Joule heating over the T_{B} of the Ir-Mn layer. Our findings offer a comprehensive understanding and a very efficient scheme in manipulating antiferromagnetic interfacial states through SOT.

ACKNOWLEDGMENTS

This work was supported by Beijing Natural Science Foundation Grant No. 2212048. This work was also supported by the NSFC Grants No. 11474272, No. 61774144, and No. 12004212, and Beijing Natural Science Foundation Key Program Grant No. Z190007. The project was sponsored by the Chinese Academy of Sciences, Grants No. QYZDY-SSW-JSC020, No. XDB28000000, and No. XDPB44000000 as well.

[1] T. Jungwirth, X. Marti, P. Wadley, and J. Wunderlich, Nat. Nanotechnol. **11**, 231 (2016).
[2] V. Baltz, A. Manchon, M. Tsoi, T. Moriyama, T. Ono, and Y. Tserkovnyak, Rev. Mod. Phys. **90**, 015005 (2018).
[3] P. Nemec, M. Fiebig, T. Kampfrath, and A. V. Kimel, Nat. Phys. **14**, 229 (2018).
[4] X. Marti, I. Fina, C. Frontera, J. Liu, P. Wadley, Q. He, R. J. Paull, J. D. Clarkson, J. Kudrnovský, I. Turek, J. Kuneš, D. Yi, J-H. Chu, C. T. Nelson, L. You, E. Arenholz, S. Salahuddin, J. Fontcuberta, T. Jungwirth, and R. Ramesh, Nat. Mater. **13**, 367 (2014).
[5] H. Yan, Z. Feng, S. Shang, X. Wang, Z. Hu, J. Wang, Z. Zhu, H. Wang, Z. Chen, H. Hua, W. Lu, J. Wang, P. Qin, H. Guo, X. Zhou, Z. Leng, Z. Liu, C. Jiang, M. Coey, and Z. Liu, Nat. Nanotechnol. **14**, 131 (2019).
[6] T. Kosub, M. Kopte, R. Huhne, P. Appel, B. Shields, P. Maletinsky, R. Hubner, M. O. Liedke, J. Fassbender, O. G. Schmidt, and D. Makarov, Nat. Commun. **8**, 13985 (2017).
[7] R. Lebrun, A. Ross, S. A. Bender, A. Qaiumzadeh, L. Baldrati, J. Cramer, A. Brataas, R. A. Duine, and M. Kläui, Nature (London) **561**, 222 (2018).
[8] X. Z. Chen, R. Zarzuela, J. Zhang, C. Song, X. F. Zhou, G. Y. Shi, F. Li, H. A. Zhou, W. J. Jiang, F. Pan, and Y. Tserkovnyak, Phys. Rev. Lett. **120**, 207204 (2018).
[9] H. Wang, C. Lu, J. Chen, Y. Liu, S. L. Yuan, S.-W. Cheong, S. Dong, and J.-M. Liu, Nat. Commun. **10**, 2280 (2019).
[10] A. S. Nunez, R. A. Duine, P. Haney, and A. H. MacDonald, Phys. Rev. B **73**, 214426 (2006).
[11] Y. Deng, R. Li, and X. Liu, J. Alloys Compd. **874**, 159910 (2021).
[12] W. Erenstein, N. D. Mathur, and J. F. Scott, Nature (London) **442**, 759 (2006).
[13] P. Wadley, B. Howells, J. Zelezny, C. Andrews, V. Hills. R. P. Campion, V. Novak, K. Olejnik, F. Maccherozzi, S. S. Dhesi, S. Y. Martin *et al.*, Science **351**, 587 (2016).
[14] P. Lin, B. Yang, M. Tsai, P. Chen, K. Huang, H. Lin, and C. Lai, Nat. Mater. **18**, 335 (2019).
[15] X. H. Liu, K. W. Edmonds, Z. P. Zhou, and K. Y. Wang, Phys. Rev. Appl. **13**, 014059 (2020).
[16] X. Liu, Y. Deng, X. Lan, R. Li, and K. Wang, Sci. China-Phys. Mech. Astron. **64**, 267511 (2021).
[17] S. A. Wolf, D. D. Awschalom, R. A. Buhrman, J. M. Daughton, S. von Molnar, M. L. Roukes, A. Y. Chtchelkanova, and D. M. Treger, Science **294**, 1488 (2001).
[18] Z. M. Zeng, J. F. Feng, Y. Wang, X. F. Han, W. S. Zhan, X. G. Zhang, and Z. Zhang, Phys. Rev. Lett. **97**, 106605 (2006).
[19] J. Nogues, J. Sort, V. Langlais, V. Skumryev, S. Surinach, J. S. Munoz, and M. D. Baro, Phys. Rep. **422**, 65 (2005).
[20] X. H. Liu, W. Liu, Z. D. Zhang, and C. F. Chang, J. App. Phys. **123**, 083903 (2018).
[21] V. Laukhin, V. Skumryev, X. Martí, D. Hrabovsky, F. Sánchez, M. V. García-Cuenca, C. Ferrater, M. Varela, U. Lüders, J. F. Bobo, and J. Fontcuberta, Phys. Rev. Lett. **97**, 227201 (2006).
[22] S. M. Wu, S. A. Cybart, P. Yu, M. D. Rossell, J. X. Zhang, R. Ramesh, and R. C. Dynes, Nat. Mater. **9**, 756 (2010).
[23] X. He, Y. Wang, N. Wu, A. N. Caruso, E. Vescovo, K. D. Belashchenko, P. A. Dowben, and C. Binek, Nat. Mater. **9**, 579 (2010).
[24] Z. P. Zhou, X. H. Liu, and K. Y. Wang, Appl. Phys. Lett. **116**, 062403 (2020).
[25] A. P. Malozemoff, Phys. Rev. B **37**, 7673 (1988).
[26] B. G. Park, J. Wunderlich, X. Martí, V. Holý, Y. Kurosaki, M. Yamada, H. Yamamoto, A. Nishide, J. Hayakawa, H. Takahashi, A. B. Shick, and T. Jungwirth, Nat. Mater. **10**, 347 (2011).
[27] Y. Y. Wang, C. Song, G. Wang, J. Miao, F. Zeng, and F. Pan, Adv. Funct. Mater. **24**, 6806 (2014).
[28] Y. C. Lau, D. Betto, K. Rode, J. M. D. Coey, and P. Stamenov, Nat. Nanotechnol. **11**, 758 (2016).
[29] A. van den Brink, G. Vermijs, A. Solignac, J. Koo, J. T. Kohlhepp, H. J. M. Swagten, and B. Koopmans, Nat. Commun. **7**, 10854 (2016).
[30] Y. C. Li, K. W. Edmonds, X. H. Liu, H. Z. Zheng, and K. Y. Wang, Adv. Quantum Technol. **2**, 1800052 (2019).
[31] A. Ghosh, S. Auffret, U. Ebels, and W. E. Bailey, Phys. Rev. Lett. **109**, 127202 (2012).
[32] L. Liu, C. F. Pai, Y. Li, H. W. Tseng, D. C. Ralph, and R. A. Buhrman, Science **336**, 555 (2012).
[33] G. Yu, P. Upadhyaya, Y. Fan, J. G. Alzate, W. Jiang, K. L. Wong, S. Takei, S. A. Bender, L.-T. Chang, Y. Jiang, M. Lang, J. Tang, Y. Wang, Y. Tserkovnyak, P. K. Amiri, and K. L. Wang, Nat. Nanotechnol. **9**, 548 (2014).

[34] K. Cai, M. Yang, H. Ju, S. Wang, Y. Ji, B. Li, K. W. Edmonds, Y. Sheng, B. Zhang, N. Zhang, S. Liu, H. Zheng, and K. Wang, Nat. Mater. **16**, 712 (2017).

[35] T. Zhu, Y. Yang, R. C. Yu, H. Ambaye, V. Lauter, and J. Q. Xiao, Appl. Phys. Lett. **100**, 202406 (2012).

[36] W. Zhang, M. B. Jungfleisch, W. Jiang, Y. Liu, J. E. Pearson, S. G. E. te Velthuis, A. Hoffmann, F. Freimuth, and Y. Mokrousov, Phys. Rev. B **91**, 115316 (2015).

[37] X. Z. Zhan, G. Li, J. W. Cai, T. Zhu, J. Cooper, C. Kinane, and S. Langridge, Sci. Rep. **9**, 6708 (2019).

[38] S. Peng, D. Zhu, W. Li, H. Wu, A. J. Grutter, D. A. Gilbert, J. Lu, D. Xiong, W. Cai, P. Shafer, K. L. Wang, and W. Zhao, Nat. Electron. **3**, 757 (2020).

[39] J. Zhang, Y. Zhang, Y. Gao, G. Zhao, L. Qiu, K. Wang, P. Dou, W. Peng, Y. Zhuang, Y. Wu, G. Yu, Z. Zhu, Y. Zhao, Y. Guo, T. Zhu, J. Cai, B. Shen, and S. Wang, Adv. Mater. **32**, 1907452 (2020).

[40] P. F. Carcia, J. Appl. Phys. **63**, 5066 (1988).

[41] N. J. Gokemeijer, T. Ambrose, and C. L. Chien, Phys. Rev. Lett. **79**, 4270 (1997).

[42] J. Wang, W. Kuch, L. I. Chelaru, F. Offi, M. Kotsugi, and J. Kirschner, J. Phys.: Condens. Matter **16**, 9181 (2004).

[43] S. A. Razavi, D. Wu, G. Yu, Y.-C. Lau, K. L. Wong, W. Zhu, C. He, Z. Zhang, J. M. D. Coey, P. Stamenov, P. K. Amiri, and K. L. Wang, Phys. Rev. Appl. **7**, 024023 (2017).